MONITORING MUNICIPAL SOLID WASTE SMALL MAGNITUDE LANDFILL SETTLEMENT WITH DINSAR

Pietro Milillo[1,2], Eric J. Fielding[3], Salvatore Masi[1], Paul Lundgren[3], and Carmine Serio[1]

1. School of Engineering, University of Basilicata, Potenza, Italy; {pietro.milillo / carmine.serio}(at)unibas.it
2. Seismological Laboratory, California Institute of Technology, Pasadena, CA, USA; milillo(at)caltech.edu
3. Jet Propulsion Laboratory, California Institute of Technology, Pasadena, CA, USA; {eric.j.fielding / paul.r.lundgren}(at)jpl.nasa.gov

ABSTRACT

Municipal solid waste landfill has been suffering from well-documented, post-closure settlement over a long period of time. Settlement may lead to various undesirable phenomena such as cracks, failure of the cover system and surface ponding contamination surrounding areas and the aquifer. In this paper we highlight how differential synthetic aperture radar (SAR) Interferometry (DInSAR) is capable of monitoring landfill settlements on different spatial and temporal scales. We focus our attention on the Montegrosso-Pallareta landfill (Potenza, Italy) using COSMO-SkyMed interferometric data. Results are compared with a solid waste landfill settlement model, showing good agreement between measurements and expected deformation.

KEYWORDS

Synthetic aperture radar, interferometry, time-series analysis, landfill, settlements, COSMO-SkyMed.

INTRODUCTION

Landfills are a feasible disposal route for municipal solid waste. Post-closure monitoring of landfill areas is fundamental to keep the environment safe near landfills and the surrounding aquifer. Since the rate and magnitude of landfill deformations are usually non-uniform, it's hard to predict differential settlements. This kind of behaviour may lead to devastating consequences regarding the structural integrity of the landfill, causing severe damage to the environment. Landfill settlement is a physical phenomenon due to the presence of void spaces in the waste basin. Overlying layers tend to fill these voids resulting in a compression and then subsequently in an increase of density. This process reflects in a subsidence on the landfill surface. Short-term and long-term settlement mechanisms can be identified as cause of the landfill surface deformations such as: mechanical compression, biodegradation, creep compression, physical and chemical corrosion, interaction and consolidation (1,2,3). These mechanisms can also be divided according to the magnitude of the induced effect (Table1).

Observations and modelling of these effects have been well documented in literature (4,5,6,7). Radar techniques such as GB-SAR, InSAR, coherence detection and interferometric Digital Elevation Model (DEM) generation have been used for landfill characterization, monitoring changes in the volume and identifying waste deposits (8,9,10). These techniques are affected by several constraints as: relative stable point, implementation costs and limited spatial coverage related to the GB-SAR instrument, and spatial averaging of the coherence map considering its estimation window (11). A long span of time between subsequent InSAR acquisitions used for generating a DEM may also involve missing some relevant displacements of several meters considering a landfill just closed.

High-magnitude settlements can be monitored using DInSAR analysis. The El Monte landfill (lat. 34.017°, lon. -118.009°) Los Angeles area - California - USA) is a good example of a landfill where

DOI: 10.12760/01-2015-1-03

primary settlement mechanisms are still deforming the area (Figure 1). We use L-Band (24 cm wavelength) UAVSAR data provided by NASA covering the period January-April 2013.

Table 1: Summary table of the settlement mechanisms and their contribution to the total settlement as described in (12) and (13).

Settlement Mechanism	Term	Magnitude
Mechanical compression	Short	High
Biodegradation	Long	High
Physical/chemical corrosion	Long	Moderate
Creep compression	Short	Moderate
Interaction and consolidation	Long	Low/moderate but localized

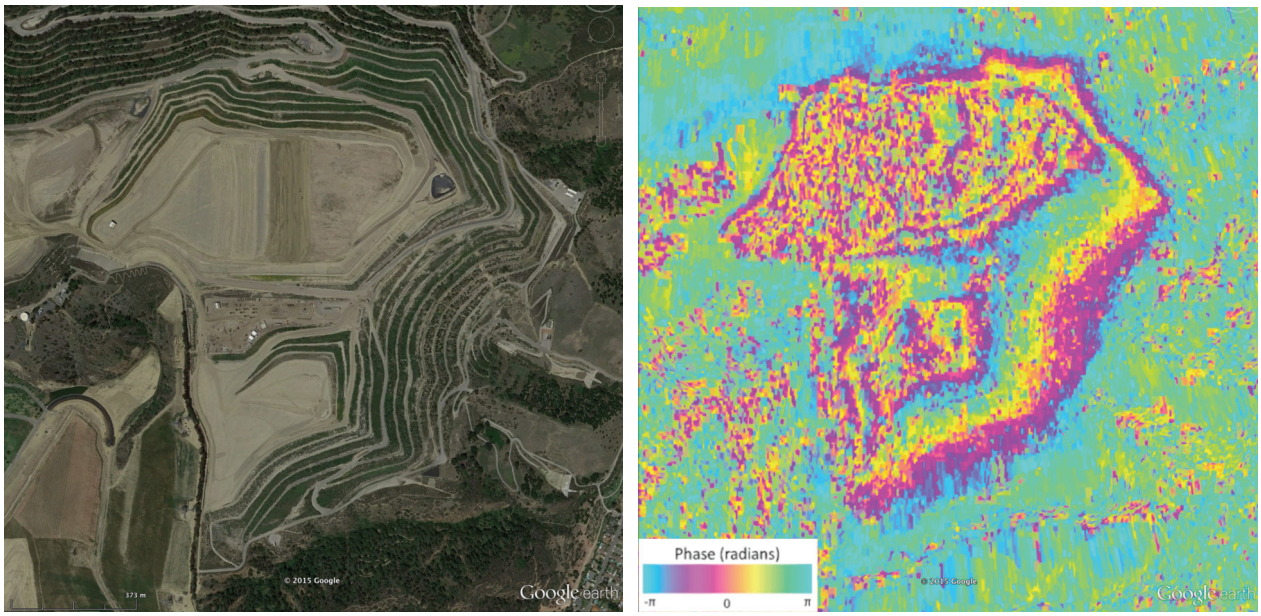

Figure 1: (Left) El Monte landfill Google Earth view. (Right) UAVSAR differential interferogram January 22 - April 4 2014. El Monte landfill is a landfill located in the Los Angeles Area. The total landfill area is approximately of 2240 ha. Due to its extension, this can easily be mapped by an L-Band SAR such as UAVSAR. Smaller landfills require better geometric resolution and sensitivity of the phase more suitable to achieve with an X band (3 cm wavelength) SAR sensors.

In this context, the second generation of SAR satellite proved to be effective near real time monitoring tool (14) able to reduce the revisit time for interferometric applications. Time-series analysis along with a constellation of high resolution SAR satellite such as COSMO-SkyMed (CSK) seems to be one of the most feasible techniques that is able to monitor low magnitude landfill settlement with millimetric accuracy.

In this paper, we highlight how low magnitude municipal solid waste landfill settlements can be monitored using DInSAR time-series analysis. Our test-site is the Montegrosso-Pallareta landfill (Potenza, Italy). Various basins closed at different times, which are affected by low magnitude post-closure settlements, characterize this landfill. We found that each basin is affected by a cumulative settlement inversely proportional to the date of closure.

We exploited the unprecedented capability of the CSK constellation to provide data with short repeat time interval (15) to characterize the spatio-temporal behaviour of the landfill settlement at different basins.

Test Site

The landfill under investigation is the Montegrosso-Pallareta landfill (lat. 40.623°, lon. 15.859°) located 2 km southeast from Potenza (Italy). The total landfill area is approximately 82 ha divided in 6 different basins (Figure 2). This landfill has not been operated recently and the different basins have been filled temporally from south to north as reported in Figure 2. We do not have short-term, high-magnitude settlement mechanism affecting the landfill. Therefore, we are able to test the DInSAR technique and determine its sensitivity to these deformations.

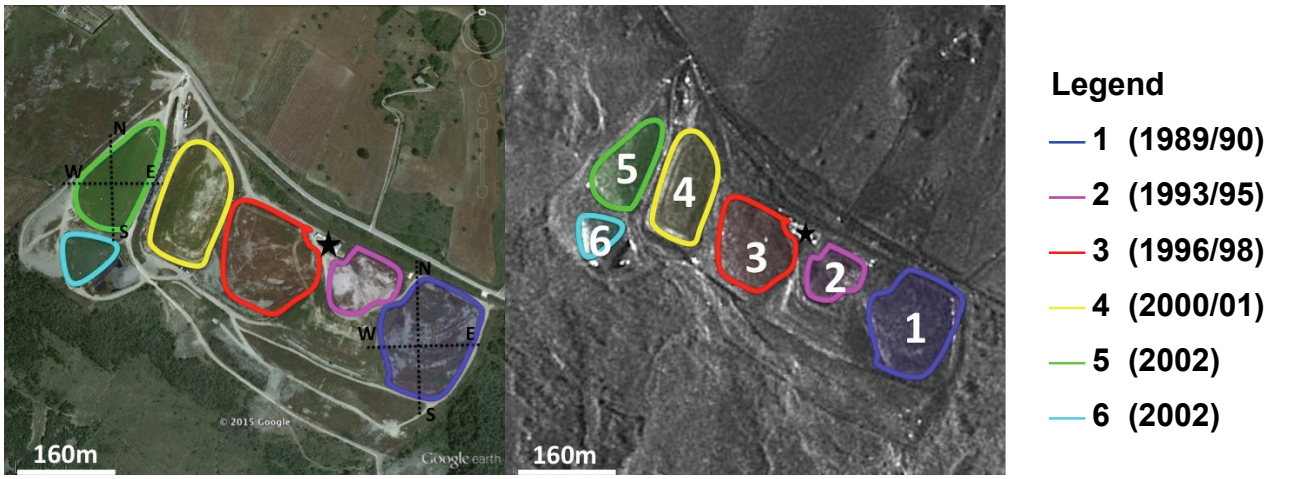

Figure 2: Montegrosso-Pallareta Landfill. (Left) optical data from Google-Earth. (Right) CSK mean amplitude of the coregistered stack. The star in indicates the reference stable point used for the time-series analysis. Legend indicates closure date from (16).

METHODS

SAR is a coherent active sensor, operating in the microwave band, which exploits relative motion between antenna and target to obtain a finer spatial resolution in the flight direction (azimuth), exploiting the Doppler effect. This way it is possible to synthetize a kilometric antenna with a few metre real antenna (5.6 metres for CSK). Pulse modulation technique is used to increase the resolution in the direction transverse to that of flight (range). By acquiring two SAR complex images with the same geometry (Figure 3A) within a certain amount of time, it is possible to interfere the two signals and extract the deformation component affecting the ground. This technique is referred to as differential interferometric SAR (DInSAR) (17). DInSAR technique is affected by several limitations such as atmospheric noise, temporal and spatial decorrelation, and DEM errors. Combining multiple SAR acquisitions is fundamental to overcome these limiting factors. Several multi-temporal techniques have been developed to combine SAR acquisitions in a time-series (18,19).

SAR Interferometry

SAR Interferometry combines the phase of two SAR scenes such that the resulting phase is proportional to the difference in range. Mathematically, an interferogram is computed pixel-by-pixel, calculating the conjugate multiplication between the first and second single look complex (SLC) SAR coregistered data. The interferometric phase can be written as:

$$\phi = -\frac{4\pi}{\lambda}\Delta\rho \qquad (1)$$

Where λ is the wavelength and $\Delta\rho$ is the difference in range. ϕ can be written as the sum of several terms:

$$\phi = \phi_{earth} + \phi_{topo} + \phi_{defo} + \phi_{atm} + \phi_{noise} \qquad (2)$$

ϕ_{earth}, ϕ_{topo} are the components due to the planet curvature and topography, respectively projected in the satellite LOS. ϕ_{defo} is the component of the Earth deformation that occurred during the sub-

sequent SAR acquisitions. ϕ_{atm} is the phase screen resulting from varying atmospheric delays. ϕ_{noise} is a nuisance term that includes decorrelation and system noise. ϕ_{earth} can be estimated given the exact position of the satellite and assuming the Earth as ellipsoidal. ϕ_{topo} can be removed using a DEM such as those produced during NASA's Shuttle Radar Topography Mission (SRTM). We consider ϕ_{atm} negligible in this particular case given the small dimensions of the test site. ϕ_{noise} temporal decorrelation effect can be reduced using the short repeat time of the CSK constellation (16 days repeat time for the single satellite) (Figure 3B). In the next paragraph we will introduce the time-series rationale for calculating ϕ_{defo}.

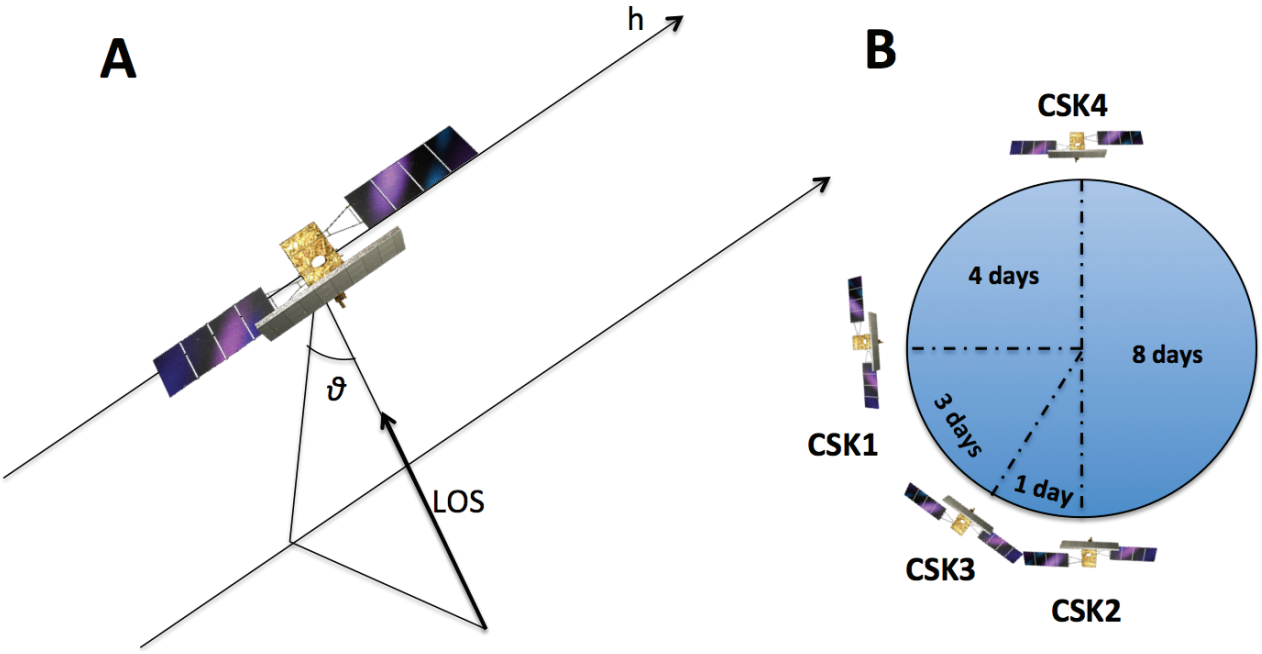

Figure 3: COSMO-SkyMed acquisition configuration. A) CSK acquisition geometry, B) presents CSK satellite positions in the orbital plane.

New small baseline approach (NSBAS)

To generate the time-series we adopted the NSBAS multi-temporal InSAR algorithm (20) using the GIAnT software (21). This time-series technique is derived by the small baseline differential SAR approach (SBAS) and has the advantage of processing a subset of the data, discarding pixel-by-pixel the single scenes with low coherence.

SBAS is a differential InSAR approach (DIFSAR) that detects Earth's surface deformations. It uses a subset of SAR images that have a mutual, small baseline below a chosen threshold. This technique fulfils the main requirement of using small baseline interferograms to avoid spatial decorrelation phenomena. The combination of multiple differential interferograms is based on a minimum norm criterion on the velocity deformation achieved via the application of the single value decomposition (SVD) method. We now describe the NSBAS algorithm starting from the SBAS rationale. For further details, we refer the readers to (17) and (19).

Considering N+1 SAR SLC data relative to the same area acquired at the chronologically ordered times

$$t = \left[t0,\ldots,tN\right]^t \tag{3}$$

We assume that each acquisition interferes with at least one other image, we have that the number of interferograms M is as in (16):

$$\left(N+1\right)/2 \le M \le N\left(N+1\right)/2 \tag{4}$$

Considering the unwrapped differential interferometric phase for a pixel (R,x) in the k-th interferogram, neglecting all decorrelation sources, we have:

$$\delta\phi_k^{diff}(R,x) = \phi(t_q,R,x) - \phi(t_p,R,x) \approx \frac{4\pi}{\lambda}\left[d(t_q,R,x) - d(t_p,R,x)\right] \quad (5)$$

Where λ is the radar wavelength, and $d(t_q,R,x)$ and $d(t_p,R,x)$ are the LOS cumulative surface deformations at the two times t_q and t_p. The following steps are carried out on a pixel-by-pixel basis on all selected coherent pixels. We can remove the (R,x) dependency and organize the unknown phase value in a vector form.

$$\phi = \left[\phi(t_1),...,\phi(t_n)\right]^T \quad (6)$$

Where the measured differential phase is organized in an M-element vector:

$$\delta\phi = \left[\delta\phi_1,...,\delta\phi_M\right]^T \quad (7)$$

The computed small baseline differential interferograms are organized in a linear model.

$$A\phi = \delta\phi \quad (8)$$

Where A is a matrix defining the small baseline combinations used. A is a linear operator composed by 0 and 1 with N columns and M rows.

A minimum-norm least squares (LS) solution is obtained using a least square scheme. This inversion scheme is iterated over the pixels where all interferograms and all acquisition dates are available.

The NSBAS estimates the LOS displacements of each pixel combining the A matrix with a set of priori constraints, combining a set or a subset of acquisition dates. The main advantage is that the selected pixel does not have to maintain coherence over the whole dataset. By releasing this constraint, it is possible to increase the number of analysed pixels.

We define these constraints as follows. For each pixel (R,x) we can write:

$$\delta\phi_i = eB_{perp}^i + \sum a_k f^k(t_i) \quad \forall\ 1 < i < M \quad (9)$$

Where f^k are a set of user defined functions, a_k are the corresponding coefficients. B_{perp}^i is the perpendicular baseline of the i-th interferogram and e is the DEM error term.

Our new system of equations becomes:

$$d = Gm \quad \Leftrightarrow \quad \begin{cases} A\phi = \delta\phi \\ 0 = \delta\phi_i - eB_{perp}^i - \sum a_k f^k(t_i) \quad \forall\ 1 < i < M \end{cases} \quad (10)$$

The resulting linear operator G can be written:

$$G = \begin{pmatrix} & & & & & 0 & 0 \\ & & |A| & & & \cdot\cdot & \cdot\cdot \\ & & & & & 0 & 0 \\ 1 & 0 & 0 & \cdot\cdot & 0 & -f^k(t_1) & B_{perp}^1 \\ 1 & 1 & 0 & \cdot\cdot & 0 & -f^k(t_2) & B_{perp}^2 \\ 1 & 1 & 1 & \cdot\cdot & \cdot\cdot & -f^k(t_3) & B_{perp}^3 \\ \cdot\cdot & 1 & \cdot\cdot & 1 & 0 & \cdot\cdot & \cdot\cdot \\ 1 & 1 & 1 & \cdot\cdot & 1 & -f^k(t_M) & B_{perp}^M \end{pmatrix} \quad (11)$$

The function f is used as a regularization function. Its contribution in the linear operator G is weighed by a parameter, small enough so that if the SBAS network is complete (i.e., no link between acquisitions is missing), the bottom part of G does not influence the inversion and is a fit to

the data. If the SBAS network is incomplete and disconnected subsets arise, then the functional form links these subsets. In our specific case *f* is a linear function.

Dataset

Dataset consist of an interferometric stack of COSMO-SkyMed Mapitaly data over Potenza acquired, starting from 2013. More information about the dataset can be found in Table 2. COSMO-SkyMed is a constellation of four X-band (3 cm wavelength) SAR satellites operated by the Italian Ministry of Defence and the Italian Space Agency (ASI). The Mapitaly project was developed by ASI and the Department of Civil Protection, with the support of e-GEOS. The goal of the project is to provide a mapping of the entire Italian territory with the CSK interferometric mode StripMap HIMAGE (HH polarization), in both right Ascending and right Descending orbit (Figure 4). We used only ascending geometry data since the expected deformation is most purely vertical and acquisitions have a better temporal continuity fundamental when looking at rapid deformation over fast decorrelating areas such as the Montegrosso-Pallareta landfill. The finer spatial resolution of X-band InSAR applications demonstrated to be very promising for monitoring both man-made structures and rural areas (22). It is possible to estimate displacement rates with a lower number of SAR scenes than higher wavelength sensors, moreover higher frequency increase both line of sight (LOS) displacement and very low displacements rates detection especially when atmospheric contributions are negligible because of the small dimensions of the test site.

Table 2: Baseline information of the Mapitaly dataset.

Master	Slave	B_{perp} (m)	Delta *t* (days)	Doppler (Hz)
2014-02-19	2013-11-15	-97.0	96	-7.1
2014-02-19	2014-01-18	-11.2	32	22.3
2014-02-19	2013-12-01	106.2	80	21.6
2014-03-23	2014-02-19	2.07	32	-25.8
2014-03-23	2013-11-15	-95.0	128	-32.9
2014-03-23	2014-01-18	-9.1	64	-3.45
2014-03-23	2013-12-01	108.3	112	-4.1
2014-01-18	2013-11-15	-85.8	64	-29.4
2014-01-18	2013-12-01	117.4	48	-0.7
2013-10-30	2013-10-14	152.4	16	-5.3
2014-01-02	2013-10-14	52.3	80	-43.6
2014-01-02	2013-10-30	-100.0	64	-38.3
2014-01-02	2013-12-01	-229.0	32	24.8
2013-12-01	2013-11-15	-203.0	16	-28.8
2013-12-01	2013-10-30	129.2	32	-63.1

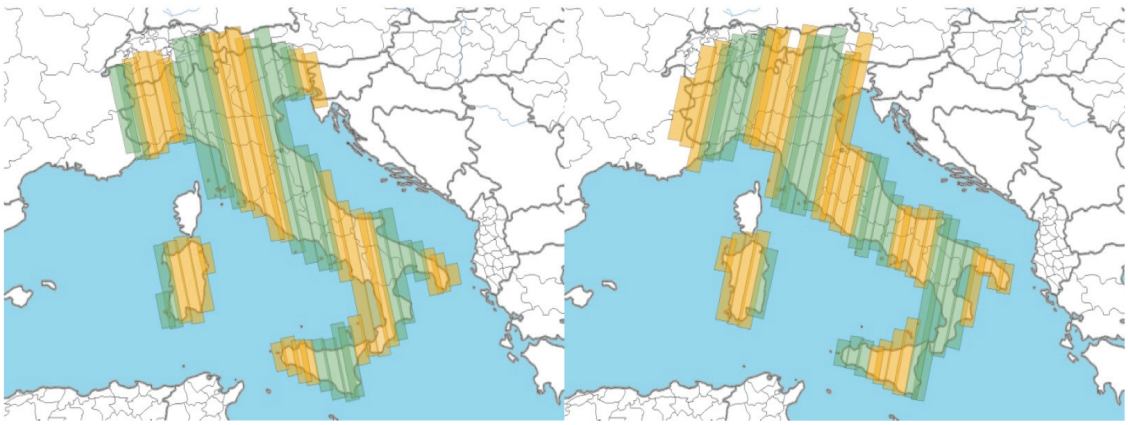

Figure 4: Mapitaly coverage, right-ascending and right-descending. For a stripmap-HIMAGE mode coverage at Italian latitude four overlapped different beams are needed. Since the COSMO-SkyMed constellation is composed of four satellites (Figure 3B), this mechanism requires assigning a beam to each satellite, thus allowing an interferometric coverage with a time baseline of 16 days.

Our dataset is composted by 10 images. We selected a network of 15 interferograms (Figure 5) discarding 2 acquisitions from our analysis. Since the Mapitaly program is still operative, we may want to hold the unused data in case of new acquisitions with temporal and perpendicular baseline within the constraints of our analysis (200 m perpendicular baseline, 4.5 months temporal baseline). We used an SRTM 90 m DEM available all over the world oversampling his grid at 10 metres. We used a multilooking factor of 5 both in azimuth and range directions to have a pixel size of about 7.5 metres. This is a reasonable trade-off considering computational load, extension of the landfill, DEM resolution and coherence improvement. Exploiting the linear dependency of the DEM error from the perpendicular baseline, we are also able to correct possible DEM errors. As all differential techniques, NSBAS requires a stable point in order to detect the amount of settlement in the landfill. We took advantage of the small building located in the landfill area, which behaved as a persistent scatterer maintaining a high coherence value in all the interferograms.

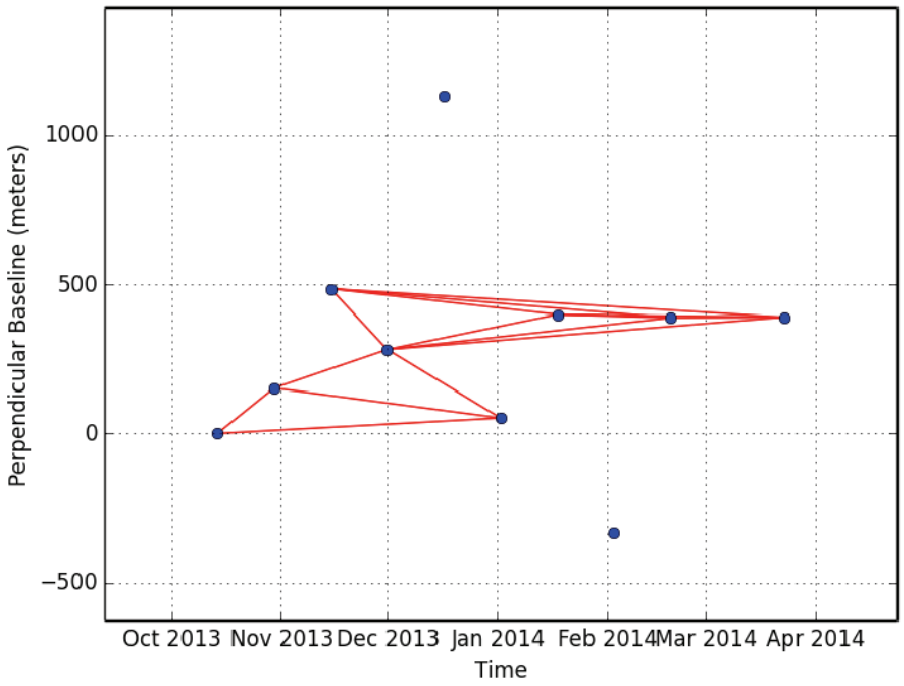

Figure 5: Baseline plot of the Potenza landfill dataset. Two acquisitions do not fulfil our selection criteria applying the NSBAS technique.

RESULTS

Landfill displacements have been calculated for each pair reported in Table 2. The displacement maps (Figure 6) show the different basin settling over time. We recorded landfill settlements directly proportional to the landfill height (Figure 7), which is compatible with the fact that the numbers of voids within the landfill increase with depth. Therefore, the compression rate at the centre is higher if compared with the border of the landfill. We noticed a various amount of landfill settlement rates for different basins (Figure 8). This phenomenon can be explained by the fact that basin 1 was the first to be closed and all the settlement mechanisms were in an advanced status when compared with basins that were filled later. It is interesting to note the time evolution of these settlements. We compared our results with modelled data from a rheological model (23) (Figure 8). This model initially developed by Gibson and Lo (23) takes into account primary and secondary compression in terms of compressive stress and time since the load application following:

$$\frac{\Delta H}{H_o} = \Delta\sigma a + \Delta\sigma b\left(1 - e^{-(\lambda/b)t}\right) \quad (12)$$

Where ΔH is the settlement; H_o the initial height of waste, $\Delta\sigma$ the compressive stress, a and b are parameters related to the primary and secondary compressibility respectively, t is the time since

load application and λ/b the rate of secondary compression. We will consider only the second term of Eq. (12) because the examined landfill is not affected by primary settlements mechanisms at the time of the SAR acquisitions, hence Eq. (12) becomes:

$$\frac{\Delta H}{H_o} = \Delta\sigma b\left(1 - e^{-(\lambda/b)t}\right) \tag{13}$$

We fitted our data using Eq. (13) finding a good agreement between the time-series and the expected trend (Table 3). Unfortunately we do not have ground truth measurements for comparing the compressive stress and the rate of secondary compression.

Table 3: Fitted values for different landfill basins.

Basin	$\Delta\sigma b$	λ/b	R^2
1	36.02 ± 1.7	0.0148 ±0.02	0.99
2	32.00 ± 2.1	0.0149 ±0.018	0.99
3	24.00 ± 1.1	0.0156 ±0.015	0.98
4	20.68 ± 1.0	0.0159 ±0.017	0.99
5	11.77 ± 1.5	0.016 ±0.010	0.97

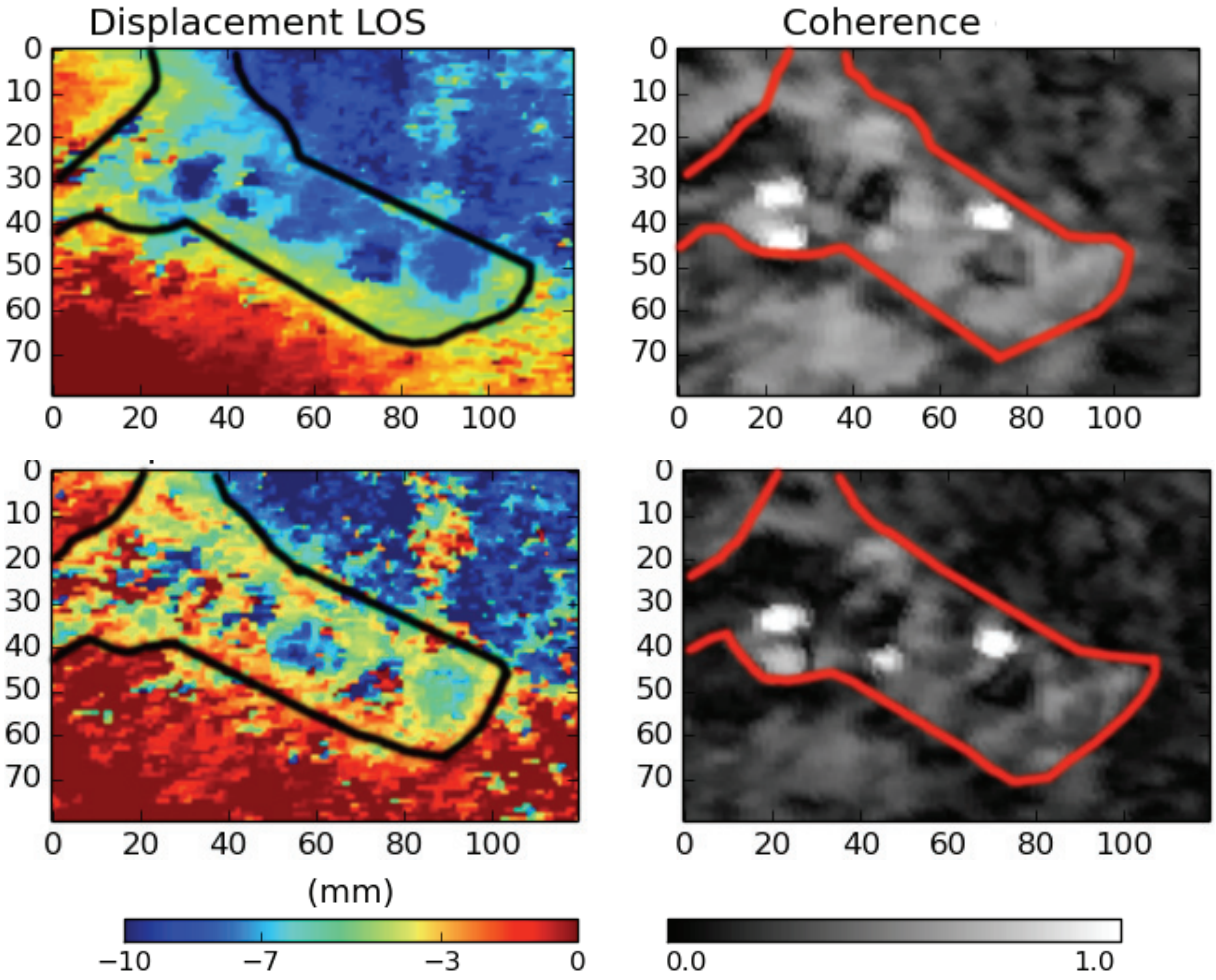

Figure 6: Differential interferogram (left) coherence map (right) related to March 23rd - January 18th 2014 (top) and February 19th – January 18th 2014 (down). Black and red lines represent the landfill border and have been drawn for localization purposes.

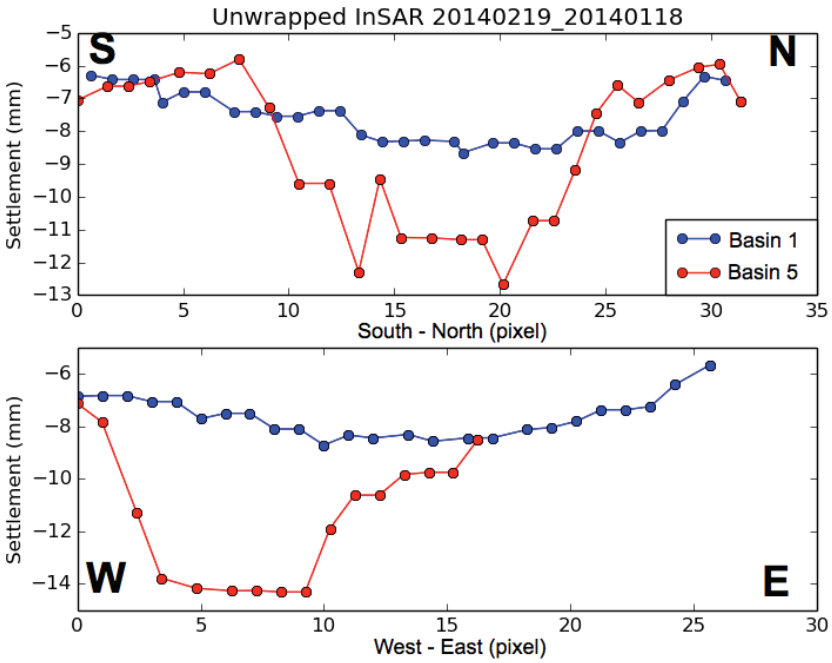

Figure 7: Differential displacement related to the February 19th January 18th 2014 interferogram. The profile shows two sections (Figure 2) of the settlement compared between basin 1 and basin 5. The different amount of displacement can be explained according to the period in which the landfill was closed. Basin 5 has been used after basin 1. A bigger settlement is then expected according to the model from Gibson and Lo (23).

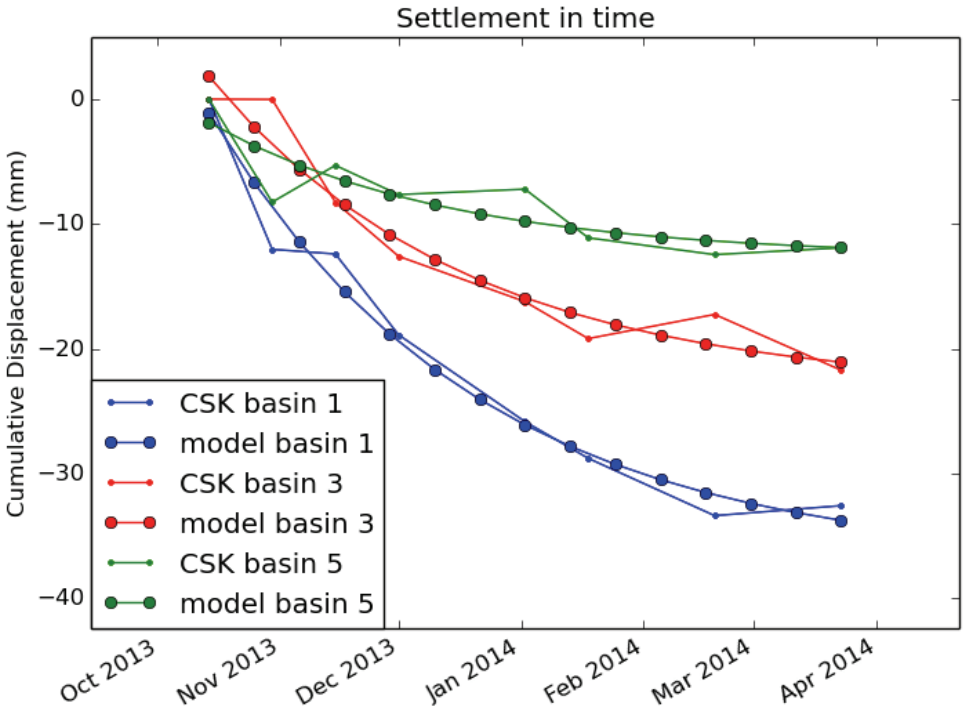

Figure 8: Cumulative CSK displacement in time fitted with the rheological model presented in (23).

SUMMARY AND FUTURE DEVELOPMENTS

We applied a well-known DInSAR time-series analysis technique on a small landfill exploiting an extensive use of SAR data acquired by the COSMO-SkyMed Mapitaly project highlighting how small magnitude landfill settlements can be monitored using SAR data. To our knowledge, this is

the first example that shows how this kind of deformation can be monitored in space and time using InSAR. We used a dataset of 10 SAR images generating a time-series of the landfill settlement. We fitted our data with the model presented in (22) taking into account only a secondary compression settlement mechanism. Although ground truth data is not available for a direct comparison of the compressive stresses and the rate of secondary compression estimated parameters, we found a good coefficient of determination between the data and the rheological model.

Further developments are needed to establish SAR time-series analysis as the foundations for a better prevention related with landfill pollution and settlements. In particular, monitoring such small deformation with longer wavelength sensor could represent a limiting factor if considering L and C band SAR sensors. Figure 8 shows an example of three interferograms from CSK, and UAVSAR covering approximately the same time period. The X band CSK sensor is more sensitive to displacement (18 cm LOS in Figure 9) when compared to the L band UAVSAR. The main drawback of the X band is the quick temporal decorrelation, which affects the coherence of the SAR signal. In our specific case this source of noise was partially healed using the COSMO-SkyMed constellation of X band SAR sensors and the NSBAS method. We believe this is the first step that aims to highlight how SAR interferometry can be used as a feasible and economical way to keep track of landfill settlements.

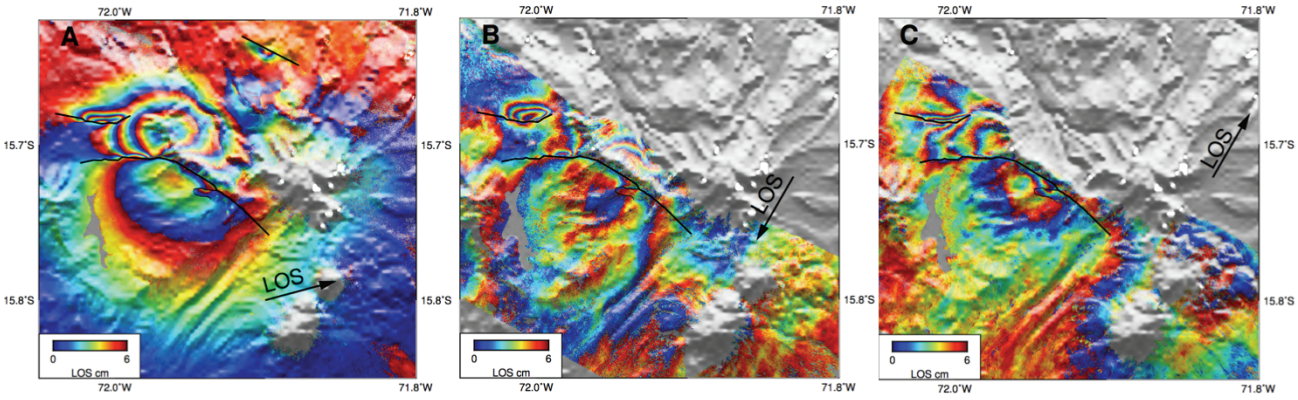

Figure 9: Interferograms related to the July 17th 2013 Sabancaya earthquake covering approximatively the same time period. Results have been unwrapped and re-wrapped at 6 cm rate for displaying purposes. A) CSK interferogram covering the period 21st April 2014 - 18th March 2013, B, C) different LOS UAVSAR interferograms spanning April 19th 2014 – March 19th 2013. As expected L band signal is noisier than X band leading to a more difficult detection of the deformation in case of small displacements.

ACKNOWLEDGEMENTS

COSMO-SkyMed data products processed at JPL under license from ASI as part of a collaborative project between CIDOT and University of Basilicata. Original COSMO SkyMed product - ©ASI - Agenzia Spaziale Italiana - (2014-2015). UAVSAR data courtesy NASA/JPL-Caltech. Part of this research was supported by the NASA Earth Surface and Interior Focus Area and performed at the Jet Propulsion Laboratory, California Institute of Technology. The work of P. Milillo was done while he was a Special Student at Caltech. Any use of trade, product, or firm names is for descriptive purposes only and does not imply endorsement by the U.S. Government. We thank the two anonymous reviewers for their constructive suggestions and comments.

REFERENCES

1 Landva A O & J I Clark, 1990. Geotechnics of waste fill. In: Geotechnics of Waste Fills – Theory and Practice, edited by A Landva & G D Knowles, pp. 86-106. ASTM STP 1070 (American Society for Testing and Materials, Philadelphia, USA) 375 pp.

2 Bjarngard A & L Edgers, 1990. Settlement of municipal solid waste landfills. Proceedings, 13th Annual Madison Waste Conference (University of Wisconsin, Madison, WI, USA) 192-205

3 Coumoulos D G & T P Koryalos, 1997. Prediction of attenuation of landfill settlement rates with time. Proceedings, 14th International Conference on Soil Mechanics and Foundation Engineering, Vol. 3, ISSMFE (Hamburg, Germany) 1807-1811

4 Belevi H & P Baccini, 1989. Long-term behavior of municipal solid waste landfills. Waste Management & Research, 7:43-56

5 Ling H I, D Leshchinsky, Y Mohri & T Kawabata, 1998. Estimation of municipal solid waste landfill settlement. Journal of Geotechnical and Geoenvironmental Engineering, 124(1): 21-28

6 Durmusoglu E, M Y Corapcioglu & K Tuncay, 2005. Landfill settlement with decomposition and gas generation. Journal of Environmental Engineering, 131(9): 1311-1321

7 Sivakumar Babu G L, K R Reddy, S K Chouskey & H S Kulkarni, 2010. Prediction of long-term municipal solid waste landfill settlement using constitutive model. Practice Periodical of Hazardous, Toxic, and Radioactive Waste Management, 14(2): 139-150

8 Ottavianelli G S., S E Hobbs, R Smith & D Bruno, 2005. Assessment of hyperspectral and SAR remote sensing for solid waste landfill management. Third CHRIS/Proba Workshop, 8 pp., ESA SP-593 (ESA-ESRIN, Frascati, Italy, June 2005)

9 Karathanassi V, C Choussiafis & Z Grammatikou, 2012. Monitoring the change in volume of waste in landfill using SAR interferometry. 32nd EARSeL Symposium Proceedings, pp. 540-551 (Mykonos Island, Greece, 21-24 May 2012) 630 pp.

10 Secker J; K E Mattar, Chen Liu, D Price & D Rowlands, 2013. RADARSAT-2 spotlight mode interferometry time series data for monitoring arctic DEW Line Clean Up. Radar Conference (RADAR), 2013 IEEE, 6 pp. (Ottawa, ON, Canada, 29 Apr – 2 May 2013)

11 Zebker H A & J Villasenor, 1992. Decorrelation in interferometric radar echoes. IEEE Transactions on Geoscience and Remote Sensing, 30(5): 950-959

12 Watts K S & J A Charles, 1999. Settlement characteristics of landfill wastes. Proceedings of the ICE - Geotechnical Engineering, 137(4): 225-233

13 Watts K S, J A Charles & H D Skinner, 2006. Predicting long-term settlement of landfills. Waste and Resources Topics, 10 pp. (last date accessed: 2014)

14 Milillo P, E Riel, B Minchew, S-H Yun, M Simons & P Lundgren, 2015. On the synergistic use of SAR constellations data exploitation for Earth science and natural hazard response. IEEE Journal of Selected Topics in Applied Earth Observations and Remote Sensing (in press)

15 Porfilio M, F Caltagirone, G F De Luca, F D'Amico, A Cecchini, F Nardone D Domizio, D Brotto, V Grimani, I Rana, D Scaranari, G Celidonio, P Inversi & M Grieco, 2011. COSMO-SkyMed full constellation orbital flexibility and interferometric capabilities. Proceedings of the 62nd International Astronautical Congress (Cape Town, South Africa)

16 Pandolfo R, S Masi & S Ascoli, undated. The evaluation of the biogas production in MSW landfill (in Italian)

17 Massonnet D & T Rabaute, 1993. Radar interferometry: limits and potential. IEEE Transactions on Geoscience and Remote Sensing, 31: 455-464

18 Berardino P, G Fornaro, R Lanari & E Sansosti, 2002. A new algorithm for surface deformation monitoring based on small baseline differential SAR interferograms. IEEE Transactions on Geoscience and Remote Sensing, 40: 2375-2383

19 Ferretti A, C Prati & F Rocca, 1999. Permanent scatterers in SAR interferometry. Geoscience and Remote Sensing Symposium IGARSS. 1528-1530

20 Lopez-Quiroz P, M P Doin, F Tupin, P Briole & J M Nicolas, 2009. Time series analysis of Mexico City subsidence constrained by radar interferometry. Journal of Applied Geophysics, 69: 1-15

21 Agram P S, R Jolivet, B Riel, Y N Lin, M Simons, E Hetland, M P Doin & C Lassere, 2013. New radar interferometric time series analysis toolbox released. Eos Transactions, American Geophysical Union, 94(7): 69-76

22 Milillo P, E J Fielding, W H Shulz & B Delbridge, 2014. COSMO-SkyMed spotlight interferometry over rural areas: The Slumgullion landslide in Colorado, USA. IEEE Journal of Selected Topics in Applied Earth Observations and Remote Sensing, 7: 2919-2926

23 Gibson R E & K Y Lo, 1961. A theory of soils exhibiting secondary compression. Acta Polytechnica Scandinavica, Civil engineering and building construction series, 296(11), 15 pp.